INSTITUTE OF PHYSICS PUBLISHING JOURNAL OF PHYSICS: CONDENSED MATTER

J. Phys.: Condens. Matter **14** (2002) 9803–9824 PII: S0953-8984(02)53317-8

Exciton and polaron dynamics in a step-ladder polymeric semiconductor: the influence of interchain order

Carlos Silva[1,3], David M Russell[1], Anoop S Dhoot[1], Laura M Herz[1], Clément Daniel[1], Neil C Greenham[1], Ana C Arias[1], Sepas Setayesh[2], Klaus Müllen[2] and Richard H Friend[1]

[1] Cavendish Laboratory, University of Cambridge, Madingley Road, Cambridge CB3 0HE, UK
[2] Max-Planck-Institute for Polymer Research, Ackermannweg 10, D-55128 Mainz, Germany

E-mail: cs271@cam.ac.uk (Carlos Silva)

Received 11 September 2002
Published 11 October 2002
Online at stacks.iop.org/JPhysCM/14/9803

Abstract

We present combined results of femtosecond transient photoluminescence (PL), femtosecond transient absorption and quasi-steady-state photoinduced absorption spectroscopy on the organic semiconductor poly-6, 6′, 12, 12′-tetraalkyl-2, 8-indenofluorene (PIF). By control of interchain order via the choice of the side-chain substituents, we have investigated its effect on exciton and polaron dynamics in this model electronic material. We show that interfaces between ordered and disordered domains play a significant role in the photophysics. At high photoexcitation fluence, a high yield (∼10%) of polarons is only observed in the ordered semiconductor. This process arises from two-step photoexcitation, first to the lowest exciton, and then to a high-energy state of opposite symmetry. In contrast, triplet exciton population is generated via sequential excitation with smaller yield (<1%) in both ordered and disordered materials. In the low fluence regime, triplet excitons are found to arise from evolution of polarons generated with low efficiency (also <1%) by diffusion-limited processes. The triplet generation yield is strongly dependent on order, with the disordered material displaying a higher yield. Polaron decay is found to be thermally activated, with a higher activation energy and lower room-temperature recombination rate in the ordered material. Furthermore, we do not find that emissive keto defects play a defining role in the PL properties of our PIF samples. Instead, absorption features of aggregate-like species, which we believe to lead to sub-gap emission, are evident in the photocurrent action spectrum of the more ordered PIF derivative.

[3] Author to whom any correspondence should be addressed.

0953-8984/02/429803+22$30.00

1. Introduction

Conjugated polymers now constitute a class of organic semiconductor materials with applications in optoelectronics [1, 2]. The observation of electroluminescence in this class of materials by Burroughes *et al* [3] has sparked intensive research activity on the physics of phenylene-based conjugated polymers, with particular emphasis on the luminescence properties. Polymeric semiconductors are attractive materials for large-scale optoelectronics applications because of their simple processability. Side-chain substitution of the phenylene backbone renders the polymer soluble, and it is possible to spin-cast semiconductor thin films on top of electrode substrates to fabricate devices. This is in contrast to competing small-molecule semiconductors such as pentacene, which can only be processed by vacuum-evaporation [4] or precursor routes [5]. This is an important advantage, since techniques such as ink jet printing can be applied to make tailored devices with highly flexible production processes [6].

Along with the advantages of simple processing, solution-cast polymer films also display morphological heterogeneity, which introduces the disadvantage of a wide distribution of intramolecular configurations and intermolecular interactions. Disorder introduces several challenges for the implementation of optoelectronic devices, because the electronic properties of polymeric semiconductors are affected sensitively by film order. A striking example of this is charge transport. Regioregular polythiophene, for example, displays field-effect mobilities that vary by over two orders of magnitude, depending on the microscopic orientation of interchain π stacks with respect to source and drain electrodes in field-effect transistor architectures [7]. Time-of-flight hole transport in polyfluorene (PF) derivatives has also been found to be strongly dependent on morphology [8]. Charge photogeneration branching ratios [9, 10] and singlet exciton bimolecular annihilation rate constants [11] correlate with interchain order.

Interchain interactions are generally considered to be detrimental to the operation of certain devices, such as light-emitting diodes (LEDs), because they decrease the luminescence efficiency, as well as introduce sub-gap emission, assigned to aggregate or excimer species, that contaminates the intrachain emission spectrum [11–22]. For example, LED device efficiency, as well as turn-on voltage, is dependent sensitively on the solvent from which the active layer is spin-cast, the speed at which the film is spun and the temperature of the solution during casting [11, 23]. Intra- and interchain thermodynamic conformations adopted in solution and transferred to the solid state, and those achieved during the casting process controlled by casting parameters, determine the ultimate performance of the device. There is therefore broad interest in the photophysical and physicochemical properties of interchain emissive species within the field of polymer electronics.

Efforts to reduce the interchain red-shifted emission have concentrated on preventing significant interchain π–π interactions by modification of the side-chain substituents with sterically-demanding alkyl groups [24–26], attachment of bulky end groups [27], use of cross-linkable groups [28, 29] and copolymerization with molecular co-monomers [30, 31]. All of these synthetic efforts have demonstrated that, when interchain interactions are discouraged, the relative contribution of red-shifted emission is suppressed.

While the presence of sub-gap emission has been correlated with excimer/aggregate species in polyphenylenevinylene (PPV) derivatives, it has been suggested in the literature, initially by Bliznyuk *et al* [32] and Lee *et al* [33], and more recently by List *et al* [34] and Lupton *et al* [35], that a contribution to green emission (about 2.3 eV) in PFs arises from emission of photochemical defects consisting of discrete fluorenone units, populated by resonance energy transfer from PF states. In fact, [34] and [35] question entirely the assignment of the green emission to aggregate-like (or excimer) species. In such a scenario, the yield of sub-gap emission is determined by the concentration of keto defect sites, and by the ability of excitons

to encounter the defects within its lifetime, determined in turn by the morphology-dependent exciton mobility [35].

This paper focuses on the role of interchain order on the photogeneration and decay kinetics of singlet and triplet excitons, and polarons, in a model conjugated polymer. We have previously investigated the time-integrated photoluminescence (PL) characteristics of poly-6, 6′, 12, 12′-tetraalkyl-2, 8-indenofluorene (PIF) [36, 37]. PIF is a step-ladder polymer with monomers consisting of three planarized phenyl rings, and is an intermediate between ladder-type poly-*p*-phenylene (LPPP), which has a completely planarized phenylene backbone, and PF. Modification of aliphatic side chains has been shown to result in dramatic changes in film topography [26, 36] and we have assigned sub-gap emission to aggregate states [37]. We re-examine this assignment in light of recent findings of fluorenone defects in PF [32–35] and conclude that such defects do not play a defining role in the steady-state spectroscopy of PIF.

We reported that resonant sequential excitation from the ground state to a high energy excited state, with the lowest exciton as an intermediate, leads to polarons via exciton dissociation [38]. Here, we discuss the dependence on two-step exciton dissociation mechanisms on morphology, and find that polarons are generated with high yield (10%) in films with high degrees of order, but with much lower yield in more disordered films. In contrast, triplet excitons are photogenerated by sequential excitation with the yield weakly dependent on film order (<1%). The singlet exciton, triplet exciton and polaron decay dynamics are influenced by the surface area of interfaces between domains of different order. We present a comprehensive picture of the photophysics in this model phenylene-based conjugated polymer by combining ultrafast and quasi-steady-state spectroscopies with access to kinetic information spanning femtosecond to millisecond timescales.

2. Experimental details

The synthesis of PIF is described elsewhere [39]. Thin-film (∼100 nm) samples were spun from 15 g l^{-1} solutions of anhydrous *p*-xylene (Aldrich) and were investigated as-spun. Solutions were prepared under a nitrogen environment using standard syringe techniques and films were spun in a nitrogen glove box.

Ultrafast measurements were carried out with one of three techniques. Transient PL measurements in solution were made by time-correlated single-photon counting (TCSPC). The 88 MHz pulse train from a Ti:sapphire oscillator (KMLabs TS, pumped by 4.5 W, 532 nm output from a Spectra-Physics Millennia V) was frequency doubled to 3.1 eV in a 0.5 mm β-barium borate (BBO) crystal. The residual fundamental was directed towards a fast Si photodiode and used as the stop signal for the TCSPC electronics running in reverse mode. The frequency-doubled beam was attenuated and directed to a spectrometer (Edinburgh Instruments Lifespec-ps) with the sample solution (0.15 g l^{-1} concentration) in an anaerobic solution cell. The detection system was a microchannel plate photomultiplier tube (Hamamatsu Photonics) coupled to TCSPC electronics (Edinburgh Instruments VTC900 plug-in PC card). The instrument response function of the apparatus was measured to be 60 ps FWHM. To measure PL dynamics with higher time resolution in thin films, fluorescence up-conversion techniques were applied. Samples in a dynamic vacuum of 1×10^{-5} mbar were photoexcited with the second harmonic output (3.1 eV) of a second Ti:sapphire oscillator (Coherent Mira) operating at 76 MHz. The laser fluence used for these experiments was 30 nJ cm^{-2}. Fluorescence emitted from the sample was up-converted in a β-BBO crystal using the residual fundamental pulses as a gate. Sum-frequency photons were directed into a monochromator and detected via single-photon counting. The spectra were corrected for the response of the apparatus measured using a tungsten lamp of known emissivity. The

instrument response in this experiment was 400 fs FWHM. Femtosecond transient absorption spectroscopy was implemented to monitor the population of non-emissive photoexcitations in femto-and picosecond timescales. The experimental apparatus has been described in detail elsewhere [40] and consists of a dye-amplified Ti:sapphire laser system operating at a repetition rate of 1 kHz. The pump beam at 3.18 eV was focused on the sample to a $\sim$125 μm spot. The weaker probe beam, consisting of a single-filament white-light continuum generated in a sapphire disc, was focused to $\sim$50 μm in the same region of the sample after passing through a computer-controlled variable optical delay. Both pump and probe beams were horizontally linearly polarized. Spectrally resolved measurements of the fractional change in probe transmission due to the pump pulse ($\Delta T/T$) were performed with a 0.25 m spectrometer and a Peltier-cooled CCD camera (Wright Instruments). The chirp across the white-light continuum was numerically corrected using an empirical determination of the dispersion. Alternatively, single probe-wavelength measurements were made by detecting a spectrally narrow portion of the dispersed probe beam with a pair of Si photodiodes measuring the probe light transmitted through the sample and a reference beam, using lock-in techniques. The sample was maintained under a dynamic vacuum of $<1 \times 10^{-5}$ mbar.

Photocurrent action spectra were measured with diodes prepared by spin-coating from solution onto glass substrates coated with indium–tin oxide (ITO). Aluminium contacts were deposited by thermal evaporation onto the polymer film. The devices were characterized electrically under a dynamic vacuum of 10^{-7} mbar. Photocurrent action spectra were measured with a monochromated xenon arc lamp, illuminating the diodes from the ITO side.

Continuous-wave photoinduced absorption (CW-PIA) measurements were performed with the sample mounted in a helium continuous-flow cryostat fitted with a heating element and a temperature controller, as described elsewhere [41]. The temperature was monitored separately with a calibrated Si diode located near the sample. Mechanically modulated UV lines of an argon-ion laser at 351 and 364 nm were simultaneously used as the excitation source. A monochromated 150 W halogen–tungsten lamp was the probe light source. A Si photodiode or a liquid nitrogen-cooled InSb photodiode provided detection of the probe light, depending on the wavelength range, after passing through a second monochromator. $\Delta T/T$ was measured as a function of wavelength using lock-in techniques, with the phase set to maximize the polymer PL signal in the X (in-phase) channel. Photoinduced absorption (PIA) due to long-lived excitations thus appeared as negative signals in the X channel, accompanied by a positive signal in the Y ($\pi/2$ out of phase) channel. The PL signal was subtracted by measuring it separately from the CW-PIA signal at each wavelength.

3. Results and analysis

3.1. Time-integrated photoluminescence spectroscopy

The materials investigated here are depicted in figure 1(a), with either *n*-octyl (PIFTO) or 2-ethylhexyl (PIFTEH) *R* groups. Polyindenofluorene (PIF) is a step-ladder derivative of poly-*p*-phenylene (PPP), which has an essentially planarized phenylene backbone with effective conjugation that extends over 5–6 monomer units [39]. In dilute solution, both derivatives display narrow PL spectra centred at 2.904 and 2.883 eV in PIFTEH (figure 1(b)) and PIFTO (figure 1(c)), respectively, due to the 0–0 vibronic transition, with vibronic replicas to lower photon energy. The branched ethylhexyl side chains induce increased torsional deplanarization of the conjugated backbone by steric hindrance and therefore blue shift the spectrum slightly by $\sim$20 meV. The side groups do not otherwise affect the electronic structure of the material. In the solid phase, however, the emission properties are strongly affected by the nature of the

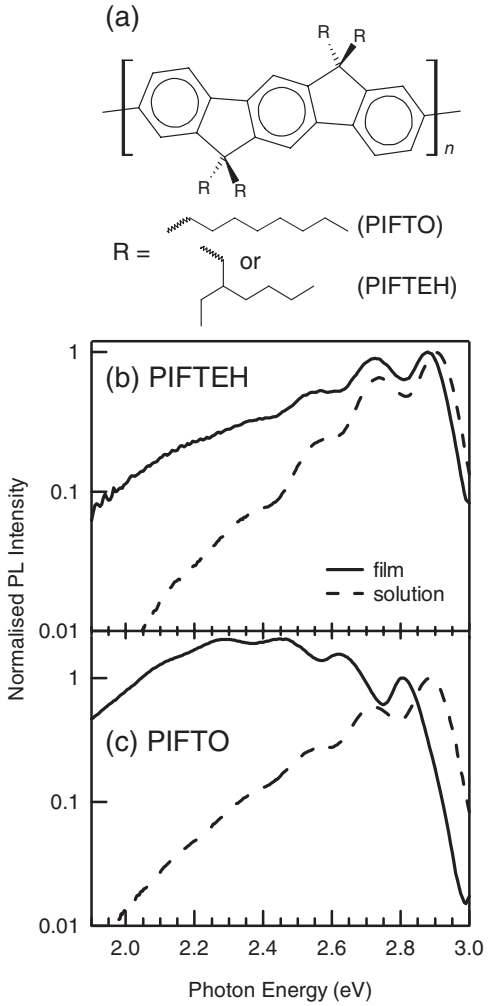

Figure 1. (a) Structure of PIF, with R either n-octyl (PIFTO) or 2-ethylhexyl (PIFTEH). Also shown are the PL spectra in 0.01 mg ml^{-1} p-xylene solutions (broken curves) and in ∼100 nm thin films (full curves) for PIFTEH (b) and PIFTO (c).

side chains. The time-integrated PL spectrum of a PIFTEH thin film is plotted in figure 1(b). The 0–0 transition centred at 2.879 eV dominates the emission and the vibronic progression has ∼0.15 eV energy spacing. In addition to the intrachain exciton emission in the blue, there is also a broad emission feature centred in the green region that is not present in the solution spectrum. The green emission dominates the steady-state PL characteristics in PIFTO (figure 1(c)). The 0–0 band is shifted further to 2.810 eV. However, the weight of the PL spectrum is centred at ∼2.36 eV. We have previously assigned the additional green emission to that from aggregate species [36, 37]. However, green spectral features in PFs have been assigned recently to emission from keto defects arising from photooxidation during measurement or during chemical synthesis [32–35]. As discussed below, emissive defects do not account quantitatively for differences in green emission in the two PIF derivatives studied here.

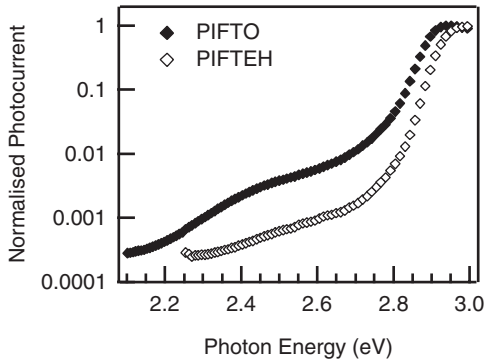

Figure 2. Comparison of the red edge of the photocurrent action spectra of PIFTO and PIFTEH. The peak external quantum efficiency of the diodes is 0.02%.

The variations in the PL characteristics in PIF with different side chains correlate with differences in the film morphology. The degree of intermolecular π interactions differs between the two materials [26, 36]. PIFTO films have been shown to form fibrillar surface topography with features that are typically ∼20 nm in diameter, while PIFTEH films show a significantly smoother surface texture, consisting of discrete features that are a factor of ∼20 less pronounced. Wide-angle x-ray scattering measurements corroborate the observation that interchain order is increased significantly in the PIFTO film.

3.2. Photocurrent action spectroscopy

Photocurrent action spectroscopy is a sensitive technique to measure the absorption of species at low concentration. A small density of aggregate sites would be sufficient to account for high yields of sub-gap emission [13]. Conventional absorption spectroscopy, and even more sensitive techniques such as photothermal deflection spectroscopy, would not be able to unravel aggregate absorption features. Figure 2 compares the photocurrent action spectra of PIFTO and PIFTEH in the red edge of the absorption spectrum. PIFTEH displays an exponential rise in photocurrent up to ∼2.7 eV, with a main feature that matches the fraction of absorbed photons at higher photon energies. PIFTO, on the other hand, displays a broad additional feature peaked at ∼2.4 eV, which is ∼6 times larger than in PIFTEH. This observation is consistent with direct absorption of aggregates, with higher dissociation probability and/or higher polaron mobility, in PIFTO. Keto photochemical defects are believed to be localized [35] and should not lead to an increased photocurrent, as they should act as carrier traps.

3.3. Time-resolved spectroscopy

3.3.1. Transient photoluminescence spectroscopy. We have employed transient PL spectroscopy with femtosecond time resolution in order to investigate the singlet exciton dynamics in PIF. Time-resolved PL spectra for PIFTEH and PIFTO films, at various delays after photoexcitation near the peak of the (π, π^*) absorption, are displayed in figure 3. The early-time (2 ps) emission spectra are similar in both materials, consisting of a 0–0 main peak and vibronic progression. Other than a small blue-shift arising from nonequilibrated excitons, the early-time PL spectra resemble their respective steady-state solution-phase spectra. Furthermore, the PL spectral evolution is similar for both materials at photon energies higher than 2.5 eV, where intrachain exciton emission dominates. However, the spectral

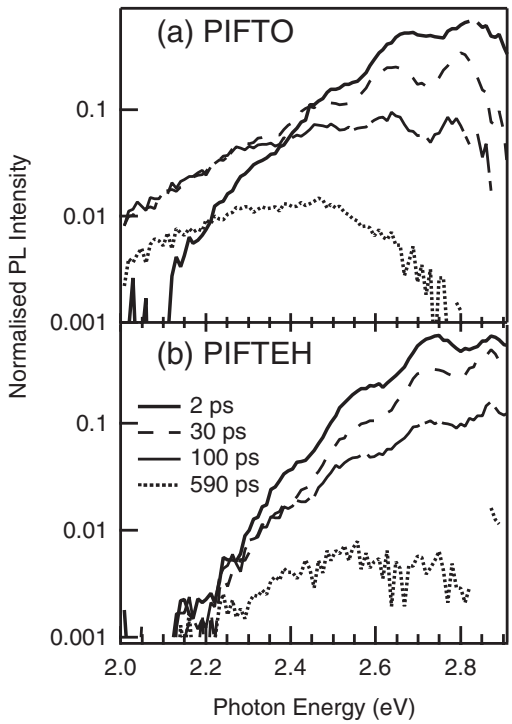

Figure 3. Time-resolved PL spectra of PIFTO (a) and PIFTEH (b) thin films at various delays after excitation, shown in the legend in part (b).

evolution at lower photon energies differs for the two materials. While there is essentially no initial PL signal in either sample at 2.1 eV, for example, a significant signal surviving on the nanosecond timescale builds up in PIFTO, but to a much lesser extent in PIFTEH. At the longest delay shown in figure 3 (590 ps), the PL spectra are dominated by emission from aggregate states in PIFTO. The vibronic peaks associated with intrachain exciton emission are still visible in PIFTEH, however.

It is possible to obtain the aggregate emission spectrum by scaling the time-integrated PL spectrum (figure 1) to coincide with the early-time spectrum in figure 3 at the 0–0 transition, shifting the latter in photon energy to account for the fact that excitons at early time have yet to undergo full thermalization and subtracting the two spectra. This procedure in effect removes the contribution from intrachain emission from the overall time-integrated spectrum. The time-integrated aggregate spectra for PIFTO and PIFTEH are displayed in figure 4. We emphasize that the aggregate spectra are normalized to the peak intensity here, but the actual intensity of the residual green emission is different in the two materials. The contribution of green emission to the total time-integrated PL spectrum is 80 and 45% in PIFTO and PIFTEH, respectively [37]. The time-integrated spectrum of PIFTO peaks at ∼2.3 eV and displays vibronic structure. PIFTEH aggregate emission peaks at ∼2.5 eV, with some vibronic structure also evident. These spectra cannot contain significant fluorenone contribution because such a large shift between the emission of these is not expected in the two materials; samples with known presence of keto defects, prepared by a variety of research groups and presumably with different parameters (solvent, spin speed, etc), which therefore ought to have varying film morphologies [11], show identical green emission spectra [32–35].

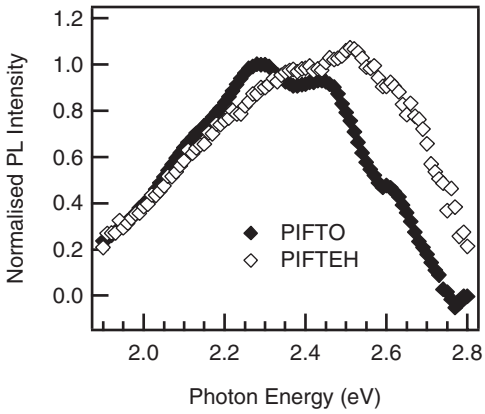

Figure 4. Comparison of the time-integrated aggregate PL spectra for PIFTO and PIFTEH.

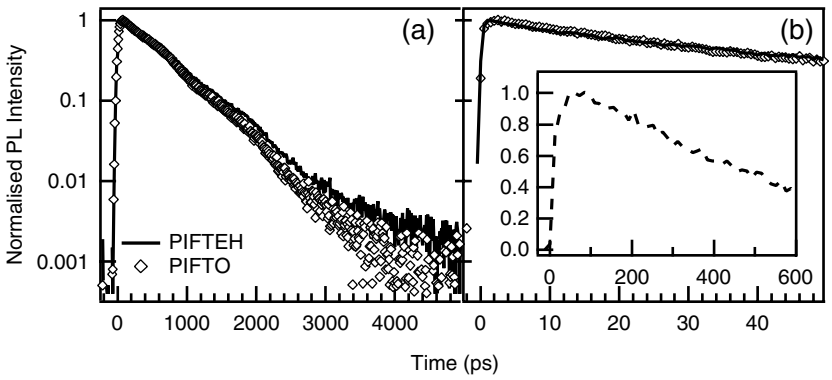

Figure 5. Comparison of the PL decay dynamics of PIFTO (full curves) and PIFTEH (open diamonds) in 0.15 mg ml^{-1} solution in *p*-xylene (a) and in thin films (b). PL at 2.82 eV photon energy was recorded for the solution-phase measurements of both materials, while the solid-phase measurements were carried out at 2.74 eV (PIFTEH) and 2.68 eV (PIFTO) photon energies. The inset displays the PL dynamics in a PIFTO film at 2.11 eV.

A comparison of PL transients is displayed for PIFTO and PIFTEH in figure 5. In moderately dilute solution (figure 5(a)), both materials exhibit exponential decay, with a time constant of 520 ps. On the other hand, the thin-film PL decay near the 0–0 peak (figure 5(b)) at short delays occurs with an exponential time constant of 35 ps. On longer timescales (not shown), PIFTEH displays a residual tail in the blue region. The growth of green emission (see inset) is correlated with the rapid decay in the blue spectral region, indicating energy transfer from intrachain exciton to aggregate states. Note that the lifetime at 2.1 eV is 860 ps.

3.3.2. Transient absorption spectroscopy. We have reported in a previous publication that in PIFTO it is possible to access high-energy states by resonant sequential excitation during the pumping process if sufficiently high fluence is used [38]. We focused on the two-step photogeneration mechanism of polarons and showed that high-energy excitonic states dissociate promptly with ∼10% effective yield. Here, we compare the two-step photoexcitation products (polarons and triplets) in PIFTO and PIFTEH and explore the consequences of enhanced interchain order.

Table 1. Saturation fluence of the $t = 0$ transient absorption signal at various photon energies, defined by $\Delta T/T \propto 1 - \exp(-\Phi/\Phi_{sat})$, where Φ is the pump fluence (see figure 6).

Photon energy (eV)	PIFTO Φ_{sat} (μJ cm^{-2})	PIFTEH Φ_{sat} (μJ cm^{-2})
2.64 (SE)	31.7	41.1
2.14 (PA_2)	411	51.3
1.49 (PA_1)	96.6	190.3

The early-time ($\leqslant$1 ps) transient absorption spectra of PIF, presented in earlier publications [36, 38], display probe-induced stimulated emission (SE) at higher photon energies than 2.3 eV. To lower photon energies, the spectra display two PIA features at $\sim$1.5 (PA_1) and $\sim$2.1 eV (PA_2) assigned to absorption of the $1B_u$ state. At low pump fluence ($<$30 μJ cm^{-2}), the transient absorption spectrum decays uniformly [36]. On the other hand, at sufficiently high pump fluence, where the $1B_u$ exciton density is saturated, we observe different decay rates in different spectral regions. Long-lived (in the nanosecond timescale) PA features persist after decay of the SE signal, which we assign to absorption of polarons around 2 eV and absorption of triplet excitons at 1.5 eV [38] (refer also to section 3.4). Figure 6 compares the pump fluence dependence of the initial ($t = 0$) SE signal at the 0–1 vibronic peak, the PA_1 signal (superimposed absorption of singlet and triplet states) and PA_2 signal (superimposed absorption of singlet and polaron states). In both materials, the SE signal saturates with a pump fluence above $\sim$35 μJ cm^{-2} (see table 1). The PA signal at 1.5 eV displays a significantly higher saturation fluence in both materials ($\sim$100 μJ cm^{-2}). Triplet exciton absorption occurs at this photon energy, therefore this species must be generated by accessing a high-energy singlet state by sequential excitation, with the lowest exciton as an intermediate and prompt ($<$100 fs) conversion to the triplet manifold. This process becomes important above pump fluences that lead to $1B_u$ exciton saturation.

In contrast, the $t = 0$ PA signal at 2.1 eV displays a significant difference in the fluence dependence between the two materials. PIFTO displays a high saturation fluence because polarons are generated through two-step dissociation of high-energy excitons [38]. PIFTEH, on the other hand, displays the same saturation fluence for this initial PA and SE. Therefore, the fate of the high-lying exciton differs in the two materials, demonstrating that interchain interactions are important in mediating exciton dissociation.

The evolution of the $1B_u$ exciton density, n_{ex}, is described by

$$\frac{dn_{ex}}{dt} = R(t)n_g - \frac{n_{ex}}{\tau_{ex}} - \beta_{ex}n_{ex}^2 - \varphi R(t)n_{ex} \tag{1}$$

where

$$R(t) = \frac{\sigma_g f_{pu}}{\sqrt{2\pi}\chi_{pu}} \exp\left[-\frac{t^2}{2\chi_{pu}^2}\right] \tag{2}$$

is the pump rate constant. Here n_g is the $1A_g$ ground-state chromophore density, σ_g is the $1B_u \leftarrow 1A_g$ absorption cross section, f_{pu} is the pump photon flux and χ_{pu} defines the pump pulsewidth. The second and third terms define the unimolecular and bimolecular exciton decay rates, respectively. The final term describes the rate of sequential excitation from $1B_u$, where the leading edge of the pump pulse generates the low-lying states and the trailing edge re-excites them to a dissociative state. The parameter φ represents the effective yield of exciton dissociation by sequential excitation and is the product of the true absolute yield and the ratio of excited-state and ground-state absorption cross sections. In this model, we assume that high-energy exciton dissociation is fast compared to the pulse width (of order 100 fs) and that the internal conversion from that state is equally fast.

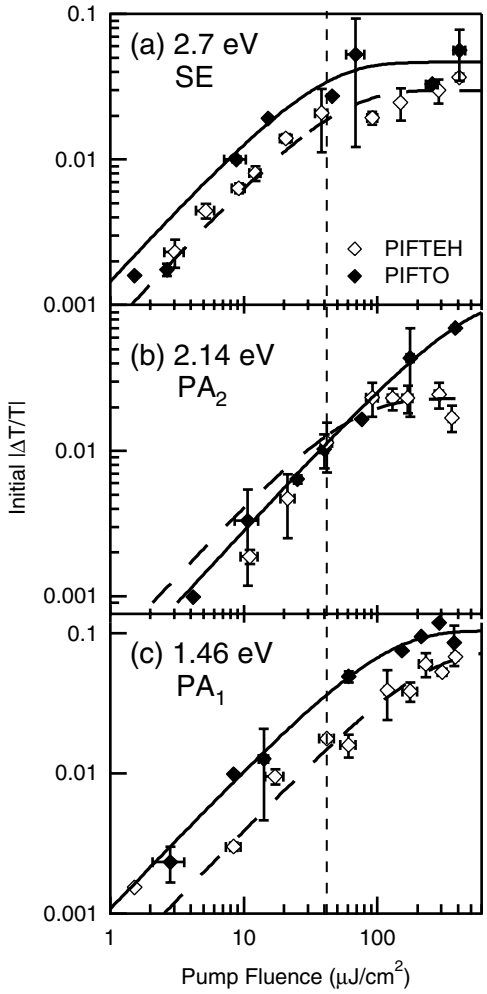

Figure 6. Initial ($t = 0$) absolute transient absorption signal as a function of pump fluence for PIFTO and PIFTEH at 2.7 (a), 2.14 (b) and 1.46 eV (c) probe photon energies. Plotted are the total initial amplitude obtained from fitting femtosecond absorption transients to a multiexponential function convoluted with the instrument response function (see [36]), measured by two-photon absorption in a CdS crystal. The curves through the data are fits to a saturation expression of the form $(1 - \exp(-\Phi/\Phi_{sat}))$, where Φ is the laser fluence and Φ_{sat} is the saturation fluence. The parameters Φ_{sat} are given in table 1. The broken curve marks a pump fluence of $\sim$40 μJ cm^{-2}, corresponding to $1B_u \leftarrow 1A_g$ photophysical saturation.

Once sequential excitation is achieved, the resulting state may undergo dissociation into triplet excitons or polarons. The dynamics of these products are governed by

$$\frac{dn_t}{dt} = \kappa\, \varphi R(t) n_{ex} - \frac{n_t}{\tau_t} \tag{3}$$

where κ is the fraction of sequentially excited states that produces triplets. The rest either dissociate into polarons (with lifetime τ_p) or undergo rapid radiationless decay.

The ground state population density, n_g, was chosen so that the absorption cross section led to the correct experimental initial SE saturation fluence given the measured ground-state

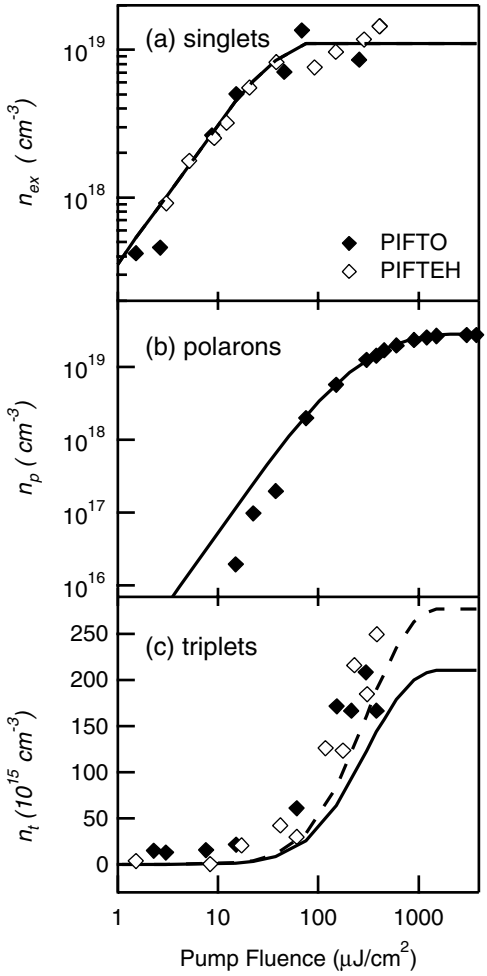

Figure 7. Model fits to the experimentally measured population density of singlets (a), polarons (b) and triplets (c) at $t = 0$ as a function of pump fluence for PIFTO (full curves) and PIFTEH (broken curves).

absorption coefficient. This was done via

$$\alpha_g = \sigma_g(n_g - n_{ex}) \approx \sigma_g n_g \tag{4}$$

which holds as long as the measurement of α_g is made far from saturation. The unique combination of σ_g and n_g that reproduced the initial SE saturation, given the measured unsaturated absorption coefficient at the pump wavelength, was used in the model. The unimolecular and bimolecular exciton decay constants were measured elsewhere [36, 37]. Therefore, the only independently variable parameters in the model are φ and κ. The value of the former dictates the saturation fluence of the dissociation species, while that of the latter determines the density of polarons and triplets achieved by sequential excitation and can thus be determined systematically.

The population densities of all species were solved using a Runge–Kutta algorithm and displayed in figure 7 (full curves). The data points are population densities extracted from the $t = 0$ transient absorption signal, obtained with the Beer–Lambert law in the form

Table 2. Summary of parameters used in the photophysical model with results displayed in figure 7. (Note: β values were determined from the pump-fluence-dependent time-integrated PL data (see [36]) [49], τ_{ex} from [37], and τ_p and τ_t were taken to be arbitrarily long compared to the timescale of the ultrafast experiment (see section 3.4).)

	PIFTO	PIFTEH
n_g (cm^{-3})	1.7×10^{19}	1.7×10^{19}
σ_g (cm^2)	2.0×10^{-15}	2.0×10^{-15}
φ	0.15	0.15
κ	5%	7%
β (cm^3 s^{-1})	2.5×10^{-8}	8.0×10^{-8}
σ_{SE} (cm^2)	4.0×10^{-16}	2.7×10^{-16}
σ_{PA_1} (cm^2)	3.0×10^{-16}	1.0×10^{-16}
σ_{PA_2} (cm^2)	1.2×10^{-16}	2.0×10^{-16}
σ_t (cm^2)	3.7×10^{-15}	3.7×10^{-15}
σ_p (cm^2)	4.4×10^{-16}	—

$$n = \frac{-1}{\sigma d} \ln\left(1 + \frac{\Delta T}{T}\right) \tag{5}$$

where d is the pump penetration depth. The cross section for SE was determined by comparing the exciton density at saturation (from the ground-state saturation fit in figure 6) with the measured $\Delta T/T$ at this fluence. Knowledge of the singlet density then allows extraction of the triplet and polaron densities from PA_1 and PA_2 signals if the absorption cross sections of all three species is known at the relevant probe photon energies. The exciton absorption cross section at 2.1 eV was calculated from the PA_2 data at low fluence as this contained only excitonic contributions. The exciton absorption cross section at 1.5 eV was also calculated from the low fluence PA_1 signal at $t = 0$, which was assumed to have a negligible contribution from triplets at low fluence (even though a long-lived triplet signal was present at later times from spin-parallel polaron recombination as described in section 3.4). Furthermore, the polaron absorption cross section reported for LPPP [42], which is closely related to PIF, was used. Finally, the triplet absorption cross section was determined from the initial PA_1 magnitude and the modelled population density. The input and output parameters for the photophysical model are presented in table 2.

3.4. Quasi-steady-state absorption spectroscopy

We have performed CW-PIA spectroscopy in order to explore the generation and decay kinetics of long-lived photoexcitations. The CW-PIA spectra for PIFTO at room temperature (part (a)) and 10 K (part (b)) are displayed in figure 8. At room temperature, the in-phase (X) channel signal (full curve) is completely dominated by a PIA (negative) signal peaked at 1.87 eV, which has been observed for related step-ladder PPP derivatives, such as PF [9] and L-PPP [43]. This has been assigned to absorption of polarons. At this moderately low pump modulation frequency (113 Hz), approximately 25% of the X signal is present in the 90° out-of-phase (Y) channel (broken curve), indicating that the population of photoinduced polaronic species is long lived on the microsecond timescale. At low temperature, the visible signal also dominates and is slightly red-shifted to 1.76 eV. However, a narrow peak is superimposed at 1.44 eV. A similar feature has been observed in L-PPP by Wholgenannt *et al* [43] and has been assigned to PIA of triplet excitons by comparison with PIA detected magnetic resonance spectroscopy. The presence of a triplet signal at low temperature indicates that a significant quasi-steady-state

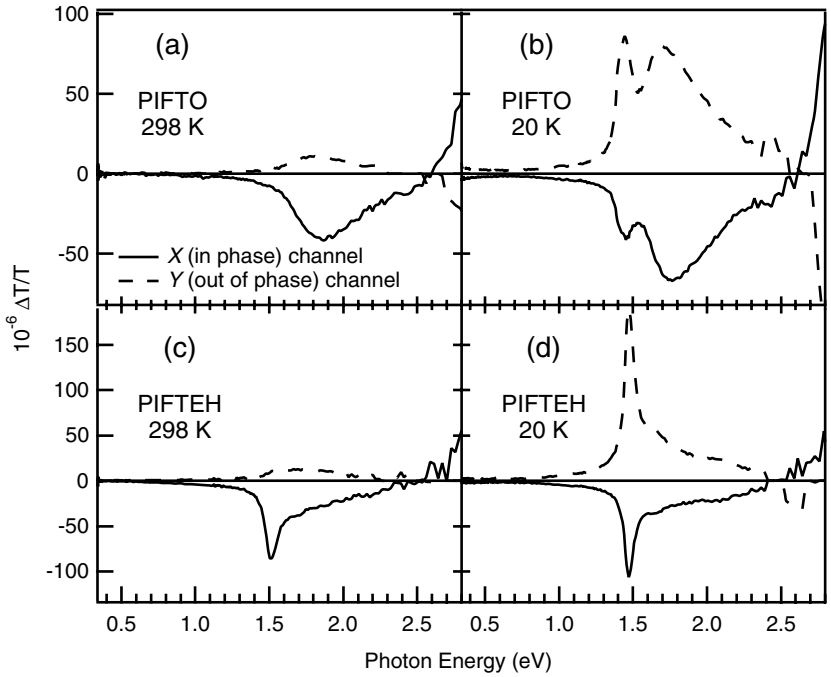

Figure 8. CW-PIA spectra of PIFTO and PIFTEH films at room and low temperatures. The full curves represent the X-channel (in-phase) signal, while the broken curves represent that in the Y channel ($\pi/2$ out of phase).

triplet density can be achieved due to the diminished importance of other radiationless decay pathways that are present at room temperature.

In contrast to the spectrum in figure 8(a), a significant population density of triplet exciton is observed in the room-temperature CW-PIA spectra of PIFTEH (figure 8(c)). The X-channel signal is dominated by the narrow signature at 1.51 eV, with a broad polaronic peak centred in the green. The triplet-induced absorption is short-lived on the microsecond timescale, as demonstrated by the lack of near-IR signal in the Y channel. On the other hand, the polaron-induced absorption feature in the visible displays similar characteristics in both materials. Significant steady-state population density of triplet excitons is generally not observed in conjugated polymers at room temperature due to competition of radiationless decay pathways with intersystem crossing dynamics and high decay rates. We note that a signal due to triplet density has also been reported by Cadby *et al* [9] in closely related PF samples. Figure 9 compares the magnitude of the CW-PIA signal (full curve) with the femtosecond transient absorption spectrum (dots) probed 800 ps after excitation. Generation of triplet exciton and polaron density is already evident on the picosecond timescale.

The long-lived photoexcitation dynamics in the CW-PIA experiment can be described by [44]

$$\frac{\mathrm{d}n}{\mathrm{d}t} = \kappa\rho G(\omega, t) - \gamma n - \beta n^2 \tag{6}$$

where n is the population density of the photogenerated species (triplet excitons or polarons), κ is the photogeneration efficiency (number of species generated per absorbed photon), ρ is the rate of photon absorption per unit volume, G is a function describing the pump modulation,

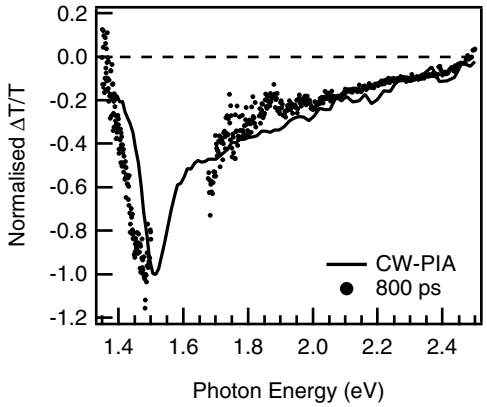

Figure 9. Comparison of the transient absorption (800 ps pump–probe delay) and the in-phase CW-PIA spectra for PIFTEH at room temperature.

ω is the pump modulation frequency and γ and β are the unimolecular and bimolecular recombination rate constants, respectively. Equation (6) does not yield a unique lifetime that is independent of laser intensity with a constant value during the entire relaxation process. However, it is possible to solve this equation under steady-state conditions, assuming that G adopts a symmetric square-wave functional form. Under these assumptions, the steady-state population density is given by [44]

$$n_s = \frac{\kappa\rho \tanh\frac{\gamma\pi}{2\omega}\tanh\frac{P\pi}{\omega}}{\frac{\gamma}{2}\tanh\frac{P\pi}{\omega} + P\tanh\frac{\gamma\pi}{2\omega}}, \qquad P = \sqrt{\beta\kappa\rho + \frac{\gamma^2}{4}} \tag{7}$$

In order to extract the parameters κ, γ and β using equation (7), we perform frequency and pump laser intensity measurements. The $\Delta T/T$ total signal, given by $R = (\sqrt{X^2 + Y^2})/T$, can be converted to population density with equation (5). We use the polaron and triplet absorption cross sections in table 2. These values are very similar to those reported for related LPPP and PPV derivatives [42, 45–47]. Using these values of σ, we plot the steady-state polaron and triplet density as a function of pump modulation frequency (figure 10) and as a function of the rate of photon absorption density (figure 11).

It has long been observed that frequency dependence data deviates from models such as equation (7) at high modulation frequency, and is commonly rationalized as arising from a broad range of lifetimes that result from a broad distribution in trapping depths in this class of disordered materials [48]. The inset of figure 10(a) shows the frequency dependence of the R signal at the peak of the polaron feature in PIFTO at room temperature. The full line through the data is a fit to equation (7). At high frequency, the signal falls as $\omega^{-0.3}$ instead of ω^{-1} as predicted by this model. Given this deviation, and because at this point there are three parameters to be extracted (κ, γ, and β), it is not possible to obtain unique fits to the frequency dependence data in the form of the inset of figure 10(a). However, at high frequency compared to the relaxation lifetime, it has been demonstrated that the photogenerated density is independent of lifetime [43] such that

$$n = \frac{\kappa\rho}{4\pi\omega} \tag{8}$$

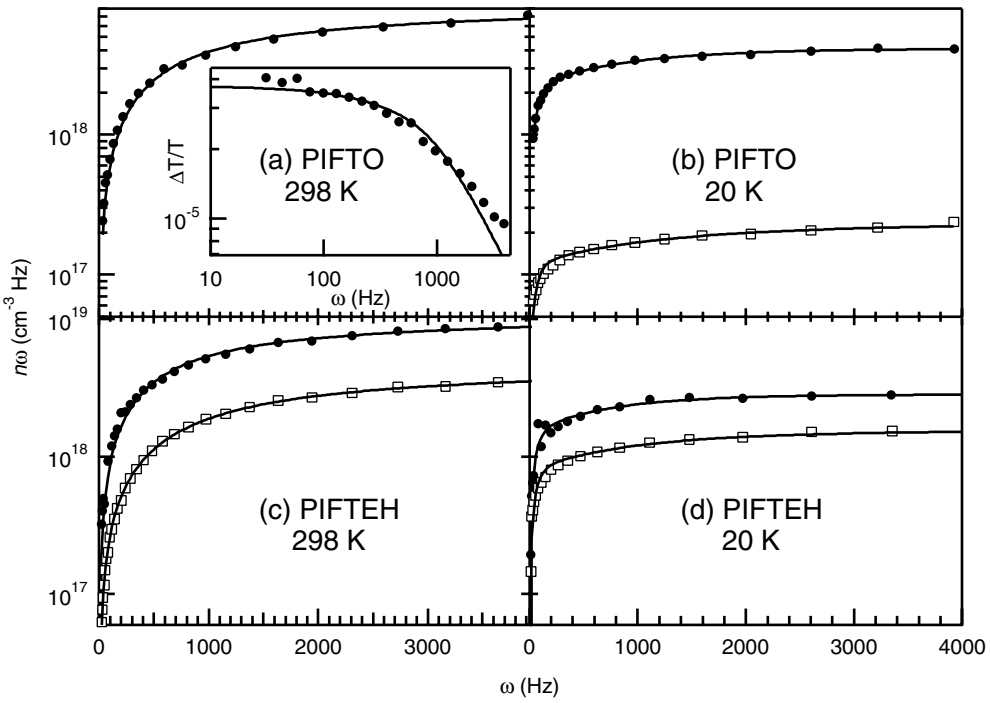

Figure 10. Frequency dependence of the product of polaron density n_p and pump modulation frequency ω for PIFTO and PIFTEH films at various temperatures. The data were collected at ∼1.8 eV (filled circles) and ∼1.5 eV (open squares) probe photon energies. The full curves are fits to a function proportional to $(2 - \exp(-x/x_{sat1}) - \exp(-x/x_{sat2}))$. The inset in part (a) displays the frequency dependence of the magnitude of the CW-PIA signal (R), with a fit to equation (7) as a continuous curve through the data.

The product of n and ω should tend to a constant value proportional to κ at high values of ω, as demonstrated by figure 10. With such a plot it is possible to extract the value of κ from the frequency dependence data. These values are presented in table 3 for polaron and triplet photogeneration in both materials at room and low temperatures. Generally, generation efficiencies are higher at room temperature than at low temperature and polarons are generated more efficiently than triplets. We also note that the polaron generation efficiency is significantly less than 1%. Using femtosecond transient absorption spectroscopy, we observe diffusion-limited growth of polaron density, on a ∼10 ps timescale, with comparable efficiencies to those found here [49]. This indicates that, under appropriate excitation conditions far from the saturation regime, polaronic species are not direct photoexcitations and contribute little to the singlet exciton dynamics.

With the generation efficiency information, we turn to the laser intensity dependence data in figure 11. The full lines are fits to equation (7) where the only variable parameters are γ and β. We emphasize that the deviation from linearity at high laser intensity is indicative of bimolecular decay processes, and therefore determined by the value of β. Thus, this fitting procedure yields unique values of the decay rate constants. A summary of the parameters derived from the fitting procedure outlined in this section is given in table 4.

At this point it is possible to determine the total pseudo-unimolecular decay rate constant of photogenerated species, $k = \gamma + n_s\beta$. The room-temperature composite polaron and triplet

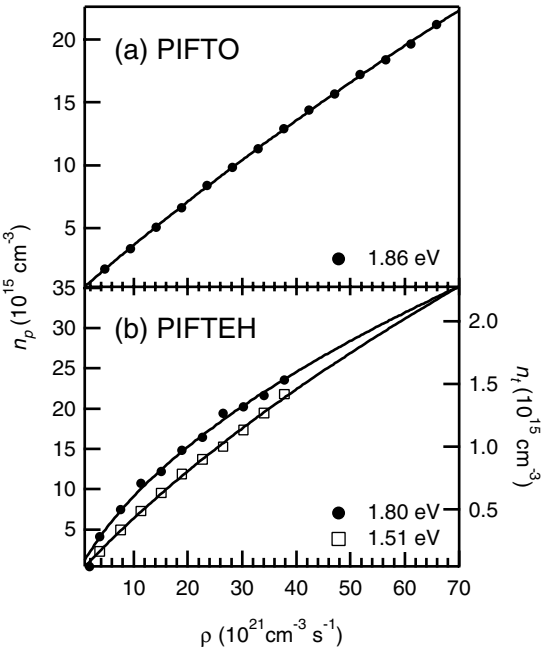

Figure 11. Polaron (left axis, filled circles) and triplet-exciton (right axis, open squares) population densities as a function of the rate of photon absorption per unit volume. The full curves are fits to equation (7).

Table 3. Summary of steady-state photogeneration efficiencies for polaron (κ_p) and triplet exciton (κ_t) densities extracted from fits to the pump modulation frequency dependence CW-PIA data in figure 10, using equation (8).

Material	Temperature (K)	κ_p	κ_t
PIFTO	298	4.1×10^{-3}	0
	20	1.9×10^{-3}	1.1×10^{-4}
PIFTEH	298	6.2×10^{-3}	3.0×10^{-3}
	20	1.6×10^{-3}	8.9×10^{-4}

Table 4. Summary of unimolecular (γ), bimolecular (β) and total ($k = \gamma + n_s\beta$) decay rate constants at room temperature, extracted from CW-PIA data in figure 11 and fits to equation (7).

Material	Species	γ (s^{-1})	β (cm^3 s^{-1})	k (s^{-1})[a]
PIFTO	Polaron	1.1×10^4	8.7×10^{-14}	1.1×10^3–1.3×10^3
PIFTEH	Polaron	4.9×10^3	2.1×10^{-14}	4.9×10^3–5.6×10^3
	Triplet	6.4×10^4	1.3×10^{-12}	6.4×10^4–6.7×10^4

[a] For n_s in the range of ρ reported in figure 11.

recombination constants are displayed in table 4. The reported range of k corresponds to n_s at the range of ρ used in figure 11.

The magnitude of k is also proportional to the ratio of Y and X CW-PIA components (for a purely unimolecular decay process k is this ratio). Therefore, scaling the temperature-dependent ratio to the room-temperature value of k derived from the fitting procedure described above allows the construction of an Arrhenius plot, as displayed in figure 12 for polaron

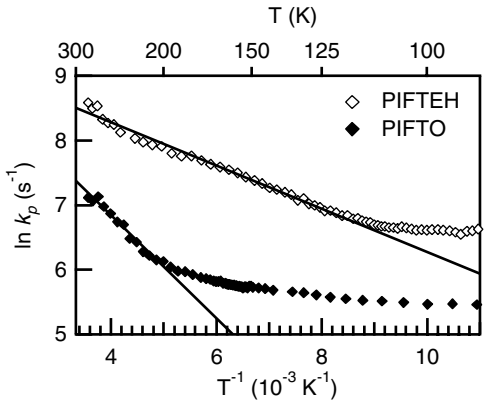

Figure 12. Arrhenius plot for polaron recombination kinetics in PIFTO measured at 1.759 eV and PIFTEH at 1.799 eV probe photon energies.

recombination. At moderately high temperature, the decay process is thermally activated in both materials but becomes more weakly dependent on temperature at low temperature as it is no longer possible to overcome the activation energy. From the data at high temperature, it is evident that the recombination activation energy is higher for PIFTO than for PIFTEH. Furthermore, polaron recombination follows Arrhenius behaviour for a larger temperature range than PIFTO. The activation energy derived from the high-temperature regime in figure 12 is 68.6 $\pm$ 7.6 and 28.8 $\pm$ 0.7 meV for PIFTO and PIFTEH, respectively. The recombination barrier for PIFTEH is only slightly larger than k_BT at room temperature, which is consistent with the higher yield of triplets by spin-parallel polaron recombination than in PIFTO (table 3).

4. Discussion

We summarize the following results that emerge from our combined spectroscopic measurements on PIF.

(i) Side-chain substitution has a significant influence on the emission properties of PIF as reported in previous publications [26, 36, 37]. PIFTO and PIFTEH samples that were derived from identical chemical synthesis and solution-processing procedures exhibit large differences in the time-integrated PL spectra, as shown here in figure 1. These are correlated with both higher molecular order (probed with wide-angle x-ray scattering techniques) and mesoscopic order (investigated with atomic force microscopy) in PIFTO [26]. On a molecular length scale, clear signatures corresponding to long-range order in 4.2 and 12.6 Å characteristic length scales are observed in PIFTO, with only weak signatures observed in PIFTEH [26]. In addition, PIFTO forms fibrillar structures that extend to the μm level, with a characteristic diameter in the $\sim$20 nm length scale. Sub-gap absorption signatures, evident in the photocurrent action spectra presented in this paper (figure 2), are consistent with higher aggregate-like character in PIFTO.

(ii) The initial intrachain exciton decay rate is similar and high in both materials with respect to that predicted from the measured PL efficiencies and that measured in solution (figure 5), but PIFTEH also displays a long-lived PL tail in the blue region of the spectrum [37], thus accounting for the higher contribution of blue emission to the time-integrated PL spectrum.

(iii) High-energy states accessed by resonant sequential excitation during femtosecond excitation dissociate into polarons with high effective yield in PIFTO but not in PIFTEH (figure 6). This suggests strongly that interchain interactions are necessary for high-energy exciton dissociation. On the other hand, two-step triplet exciton generation occurs with similar efficiency in both materials.

(iv) Polaron generation efficiencies at excitation regimes where sequential excitation as above is not important, measured with quasi-steady-state PIA spectroscopy, are marginally higher in PIFTEH, but less than 1% in both materials (table 3). By comparison with femtosecond transient absorption data [49], this population density is mostly generated on a timescale of $\sim$100 ps in the low pump fluence regime. The pseudo-first-order polaron recombination time constant at room temperature is $\sim$200 μs in PIFTEH, but is $\sim$800 μs in PIFTO at moderately low intensity (table 4). Polarons must overcome an activation barrier that is a factor of $\sim$2 higher than k_BT at room temperature in PIFTO to undergo recombination, while in PIFTEH this barrier is of order k_BT (figure 12).

(v) Triplet exciton generation efficiencies are significantly higher in PIFTEH at all temperatures (table 3). If the principal room-temperature triplet generation mechanism is spin-parallel polaron recombination, this is consistent with the higher polaron decay rate and lower activation energy for polaron recombination in PIFTEH, as discussed above. At room temperature, the triplet lifetime is significantly shorter (15 μs) than that of polarons.

We first discuss the nature of the green emissive species in PIF and reassert that such emission contains a significant contribution from interchain states. Aggregate-like species have been established here in PIF, but the 2.3 eV emission in PIFTO could also contain keto defect contributions [32–35]. It may be argued that, as the fluorenone density is expected to be similar in both materials, differences in time-integrated PL characteristics are due to more effective migration towards defect sites in PIFTO. In solution, where interchain interactions are diminished significantly, this would play a lesser role. This is plausible since, as first suggested by Nguyen *et al* [50], intrachain exciton migration is a slower process. In that study, alkoxy-substituted PPV chains were isolated by incorporation into nanoporous silicate material. Femtosecond polarization anisotropy SE measurements revealed that exciton migration is less rapid than when the chains are not isolated. Similarly, we have investigated resonance energy transfer between PIF and a red-emitting perylene derivative in a dye-end-capped PIF [51]. In a moderately dilute solution, the energy transfer rate is decreased by over an order of magnitude because the interchain exciton electronic coupling, calculated quantum chemically with INDO/SCI methodologies, is correspondingly smaller. Therefore, if small changes in the interchain conformation affect drastically the exciton migration kinetics, then we would expect that a small fraction of sites containing keto defects could have different consequences in the time-integrated PL characteristics. However, the similarity of the decay rate of intrachain excitons in PIF with different side chains discounts the hypothesis that the yield of green emission is migration dependent.

An alternative explanation would be that the total number of emissive defect sites differs in the two materials. This would require PIFTO to be more susceptible to photooxidation, which is unlikely. Also, statistical copolymers of PIFTO and PIFTEH, where only 10% of the monomer units have 2-ethylhexyl side chains and the rest have *n*-octyl groups, display steady-state PL characteristics that resemble those of PIFTEH [26]. This observation is consistent with related PL measurements in PIFTO-*co*-anthracene statistical copolymers, which display a dramatic reduction of green emission, even with a moderately low ($\sim$15%) anthracene relative composition [31]. In both reports, small changes in the composition of the polymer have profound effects in the yield of green emission. Therefore, they are unlikely to arise

from differences in the rate of populating fluorenone sites, which would be present in small concentration, and with similar concentration in all of the above materials. We do not, therefore, consider that the spectral changes that correlate with molecular order arise from emissive defects but rather from aggregate-like regions associated with the sub-gap absorption features evident in the photocurrent data.

The ribbon-like surface topography of PIFTO [26] resembles that reported for PF. Teetsov and Vanden Bout have investigated nanoscale molecular ordering in PF using polarized scanning near-field optical microscopy (SNOM) [20, 21]. In those samples, two distinct interchain PL characteristics were found. The first emerged from clusters with 50–150 nm length scales, consisting of lower PL efficiency than in unclustered regions. These regions were found to be unpolarized and were thought to arise from undissolved material. On the other hand, 50–500 nm regions displaying long-range order were also evident. By side-chain modification from *n*-hexyl to *n*-dodecyl groups, the long range order was extended significantly. The authors concluded that side-chain-controlled interchain interactions induce order during the spin-casting process. Moreover, the intrachain correlation length can be modified by thermal sample treatment. By thermally cycling a related PF sample (containing *n*-octyl substituents) to 80 K and slowly reheating it to room temperature (to form the β phase), Grell *et al* [52] demonstrated, using x-ray fibre diffraction measurements, that the intrachain correlation length is increased significantly, and that red-shifted absorption features resulting from enhanced π interactions correlate with this change. Based on the structural and film-topographical similarity with PF, we expect that the PL characteristics in PIF are governed by interchain π interactions.

We now turn to the photophysics of sequentially excited states. Our initial focus was on two-step exciton photodissociation to polarons in PIFTO [38]. In a pump fluence regime, where the ground-state absorption transition is saturated, we observe a linear rise in the zero-time polaron density. This arises because the excited-state absorption cross section at the pump photon energy is significantly smaller than the ground-state absorption cross section, and therefore the saturation fluence of the excited-state absorption is higher. We have reported photophysical modelling where the only variable parameter is the effective dissociation yield, which is the product of the true high-energy dissociation yield and the ratio of excited-state to ground-state absorption cross section [38]. This value was found to be 10%, indicating that exciton dissociation in high-energy states is effective in PIFTO. In contrast, PIFTEH shows no zero-time polaron signal from two-step exciton dissociation, indicating that interchain order is important for high-energy exciton dissociation (figure 6). In PIFTEH, sequentially excited states must relax to the lowest exciton in fast timescales compared to the instrument response. This leads us to conclude that geminate polarons arising from this process are in different polymer chains and have an energetic barrier for recombination.

The dependence on interchain order of exciton and polaron dynamics on ultrafast timescales presented in this paper are in agreement with reports from other groups. Femtosecond transient absorption measurements on PF by Korovyanko and Vardeny [10] show that thermal cycling to induce the so-called β phase, as described above, enhances polaron generation and decay. In that work, the authors argue convincingly that higher order in the β phase leads to higher yields of polaron formation and that this must arise from dissociation of hot $1B_u$ excitons in adjacent polymer chain as the 3.1 eV pump photon energy is insufficient to overcome the exciton binding energy and dissociate excitons directly (this effect would occur only above 3.3 eV [9]). However, 30–300 μJ cm^{-2} pump fluences used in that work are sufficient to induce two-step exciton dissociation as outlined here, which we have also reported [40] in similar PF samples as in [10]. Therefore, the higher polaron generation efficiency in the β phase of PF reported by Korovyanko and Vardeny appears to be in agreement with this work.

The $t = 0$ triplet exciton signature, on the other hand, displays similar behaviour in the two materials. Sequential excitation always produces triplets in femtosecond timescales, as demonstrated in figure 6. The prompt triplet density is significantly lower than that for polarons, with the effective dissociation yield as described above less than 1% [49]. The weak dependence on interchain order suggests that triplet generation from high-energy excitons is principally an intrachain effect.

We do not have any information on the mechanism of ultrafast triplet generation at this point, but we note that Wohlgenannt *et al* have observed triplet photogeneration by hot singlet fission ($S \rightarrow T_\uparrow + T_\downarrow$) at high excitation photon energy ($\geqslant$3.2 eV) in LPPP. This mechanism should be operative at photon energies $E \geqslant 2E_t$, where E_t is the triplet energy, which was therefore deduced to be 1.6 eV. In those measurements, the singlet states that undergo fission are prepared by direct photoexcitation from the ground state and therefore have B_u symmetry by absorption selection rules. The states that are accessed at $t = 0$ in our measurements have the $1B_u$ exciton as an intermediate: so are A_g. It is possible that singlet fission from such states is responsible for our measurement of ultrafast triplet photogeneration.

With CW laser excitation, where such sequential processes are not operative, triplets may be generated either by intersystem crossing or from the evolution of long-lived geminate polarons [53, 54]. From low fluence transient absorption data [36], subtraction of the exciton contribution (using the SE signal) from the overall contribution at 1.5 eV [49] reveals the growth of triplet density on 200 ps timescales, which are long compared to the excited-state lifetime (figure 5). These timescales correspond to the decay of polaron density generated by exciton diffusion-controlled dissociation (with $<$1% yield), derived by subtraction of the exciton from the total signal at 2.1 eV. Furthermore, the yield of picosecond triplet signal, although significantly less than 1% in both materials, is larger in PIFTEH. Therefore, the steady-state triplet density in PIFTEH is derived from the evolution of polarons and not intersystem crossing. Similarly, by comparing triplet photogeneration action spectra with photocurrent action spectra, Cadby *et al* [9] argued that there is a clear link between polaron generation and room-temperature triplet generation in PF samples in the β phase. Finally, a combined spectroscopic approach using CW-PIA and PADMR techniques led Wohlgenannt *et al* [55] to report steady-state triplet generation by spin-parallel polaron recombination in LPPP.

The efficiency for this process is sufficiently lower in PIFTO that no discernible steady-state density is achieved. Also, Cadby *et al* [54] argued that steric effects arising from side groups affect the triplet lifetime. We note that the decay rate constant of polarons is lower in PIFTO (table 4). It is reasonable to suggest that both triplet generation via this mechanism and polaron decay are diffusion-limited. The rate-limiting process might then be polaron hopping across interfaces, which would be thermally activated. With a higher surface area of such interfaces in PIFTO, the activation energy for polaron decay is then higher in this material.

5. Conclusions

We have combined femtosecond transient PL, femtosecond transient absorption and quasi-steady-state absorption spectroscopies to explore the role of interchain order in exciton and polaron dynamics in PIF, a promising blue-emitting semiconductor conjugated polymer for optoelectronics. In an *n*-octyl substituted material (PIFTO), the interchain order is enhanced with respect to a similar material that is substituted with 2-ethylhexyl side groups (PIFTEH). We find that, in addition to the time-integrated luminescence characteristics, side-chain substitution influences the photoexcitation dynamics. In the more ordered material (PIFTO), two-step excitation to high-energy A_g states leads to a high yield of exciton photodissociation ($\sim$10%), but not in the less ordered material (PIFTEH), pointing to the importance of interchain

interactions in the dissociation process. On the other hand, a small yield of triplet exciton generation, possibly by high-energy singlet exciton fission, occurs with similar efficiency ($<1\%$) in both materials.

At low excitation power, where such effects are negligible, we find that resonance energy homotransfer (exciton migration between unsegregated regions of the sample) occurs more efficiently in PIFTEH, but heterotransfer between intrachain states and aggregate states occurs with a rate that is material-independent. Polarons are generated with very low efficiency ($<1\%$) by diffusion-limited processes, most likely by dissociation at defect sites. The evolution of these species, however, differs in the two materials. In PIFTEH, a significant density of triplet excitons is produced from polaron recombination, but occurs with negligible efficiency in PIFTO. We also measure a higher room-temperature polaron decay rate, and a lower polaron decay activation energy, in PIFTEH. We conclude that interfaces between domains of different intermolecular order play a significant role in the exciton and polaron dynamics in polymeric semiconductors.

Acknowledgments

This research was funded by the Engineering and Physical Sciences Research Council (EPSRC). CS is an EPSRC Advanced Research Fellow.

References

[1] Friend R H, Gymer R W, Holmes A B, Burroughes J H, Marks R N, Taliani C, Bradley D D C, dos Santos D A, Brédas J L, Lögdlund M and Salaneck W R 1999 *Nature* **397** 121
[2] Heeger A J 2001 *J. Phys. Chem.* B **105** 8475
[3] Burroughes J H, Bradley D D C, Brown A R, Marks R N, MacKay K, Friend R H, Burns P L and Holmes A B 1990 *Nature* **347** 539
[4] Schön J H, Kolc C and Batlogg B 1997 *J. Cryst. Growth* **182** 416
[5] Brown A R, Pomp A, de Leew D M, Klaassen D B M, Havinga E E, Herwig P and Müllen K 1996 *J. Appl. Phys.* **79** 2136
[6] Sirringhaus H, Kawase T, Friend R H, Shimoda T, Inbasekaran M, Wu W and Woo E P 2000 *Science* **290** 2123
[7] Sirringhaus H, Brown P J, Friend R H, Nielsen M M, Bechgaard K, Langeveld-Voss B M W, Spiering A J H, Janssen R A J, Meijer E W, Herwig P and de Leeuw D M 1999 *Nature* **401** 685
[8] Redecker M, Bradley D D C, Inbasekaran M and Woo E P 1999 *Appl. Phys. Lett.* **74** 1400
[9] Cadby A J, Lane P A, Mellor H, Martin S J, Grell M, Giebeler C, Bradley D D C, Wohlgenannt M, An C and Vardeny Z V 2000 *Phys. Rev.* B **62** 15604
[10] Korovyanjo O J and Vardeny Z V 2002 *Chem. Phys. Lett.* **356** 361
[11] Nguyen T Q, Martini I B, Liu J and Schwartz B J 2000 *J. Phys. Chem.* B **104** 237
[12] Jenekhe S A and Osaheni J A 1994 *Science* **265** 765
[13] Lemmer U, Heun S, Mahrt R F, Scherf U, Hopmier M, Siegner U, Göbel E O, Müllen K and Bässler H 1995 *Chem. Phys. Lett.* **240** 373
[14] Köhler A, Grüner J, Friend R H, Müllen K and Scherf U 1995 *Chem. Phys. Lett.* **243** 465
[15] Blatchford J W, Gustafson T L, Epstein A J, Vanden Bout D A, Kerimo J, Higgins D A, Barbara P F, Fu D K, Swager T M and MacDirmaid A G 1996 *Phys. Rev.* B **54** R3683
[16] Samuel I D W, Rumbles G, Collison C J, Friend R H, Moratti S C and Holmes A B 1997 *Synth. Met.* **84** 497
[17] Jakubiak R, Collison C J, Wan W C, Rothberg L J and Hsieh B R 1999 *J. Phys. Chem.* A **103** 2394
[18] Nguyen T Q, Doan V and Schwartz B J 1999 *J. Chem. Phys.* **110** 4068
[19] Nguyen T Q, Yee R Y and Schwartz B J 2001 *J. Photochem. Photobiol.* A **144** 21
[20] Teetsov J A and Vanden Bout D A 2000 *J. Phys. Chem.* B **104** 9378
[21] Teetsov J A and Vanden Bout D A 2001 *J. Am. Chem. Soc.* **123** 3605
[22] Teetsov J A and Vanden Bout D A 2001 *Langmuir* **18** 897
[23] Shi Y, Liu J and Yang Y 2000 *J. Appl. Phys.* **87** 4254
[24] Jakubiak R, Bao Z and Rothberg L J 2000 *Synth. Met.* **114** 61

[25] Setayesh S, Grimsdale A C, Weil T, Enkelmann V, Müllen K, Meghdadi F, List E J W and Leising G 2001 *J. Am. Chem. Soc.* **123** 946
[26] Grimsdale A C, Leclère P, Lazzaroni R, MacKenzie J D, Murphy C, Setayesh S, Silva C, Friend R H and Müllen K 2002 *Adv. Func. Mater.* at press
[27] Klärner G, Miller R D and Hawker C J 1998 *Polym. Prepr.* 1006
[28] Chen J P, Klärner G, Lee J-I, Markiewicz D, Lee V Y and Miller R D 1999 *Synth. Met.* **107** 129
[29] Klärner G, Lee J-I, Chan E, Chen J P, Nelson A, Markiewicz D, Siemens R, Scott J C and Miller R D 1999 *Chem. Mater.* **11** 1800
[30] Klärner G, Davey M H, Chem W D, Scott J C and Miller R D 1998 *Adv. Mater.* **10** 993
[31] Marsitzky D, Scott J C, Cheng J P, Lee V Y, Miller R D, Setayesh S and Müllen K 2001 *Adv. Mater.* **13** 1096
[32] Bliznyuk V N, Carter S A, Scott J C, Klärner G and Miller R D 1999 *Macromolecules* **32** 361
[33] Lee J I, Klärner G and Miller R D 1999 *Chem. Mater.* **11** 1083
[34] List E J W, Guentner R, Scanducci de Freitas P and Scherf U 2002 *Adv. Mater.* **14** 374
[35] Lupton J M, Craig M R and Meijer E W 2002 *Appl. Phys. Lett.* **80** 4489
[36] Silva C, Russell D M, Stevens M A, MacKenzie J D, Setayesh S, Müllen K and Friend R H 2000 *Chem. Phys. Lett.* **319** 494
[37] Herz L M, Silva C, Phillips R T, Setayesh S and Müllen K 2001 *Chem. Phys. Lett.* **347** 318
[38] Silva C, Dhoot A S, Russell D M, Stevens M A, Arias A C, MacKenzie J D, Greenham N C, Friend R H, Setayesh S and Müllen K 2001 *Phys. Rev.* B **64** 125211
[39] Setayesh S, Marsitzky D and Müllen K 2000 *Macromolecules* **33** 2016
[40] Stevens M A, Silva C, Russell D M and Friend R H 2001 *Phys. Rev.* B **63** 165213
[41] Ginger D S and Greenham N C 1999 *Phys. Rev.* B **59** 10622
[42] Haugender A, Neges M, Kallinger C, Spirkl W, Lemmer U, Feldmann J, Scherf U, Gügel A and Müllen K 1999 *Phys. Rev.* B **59** 15346
[43] Wohlgenannt M, Graupner W, Leising G and Vardeny Z V 1999 *Phys. Rev.* B **60** 5321
[44] Dellepaine G, Cuniberti C, Comoretto D, Musso G F, Figari G, Piaggi A and Borghesi A 1993 *Phys. Rev.* B **48** 7850
[45] Candeias L P, Padmanaban G and Ramakrishnan S 1999 *Chem. Phys. Lett.* **349** 394
[46] Monkman A P, Burrows H D, Miguel M D, Hamblett I and Navratnam S 1999 *Chem. Phys. Lett.* **307** 303
[47] Cleave V, Yahioglu G, Le Barny P, Hwang D H, Holmes A B, Friend R H and Tessler N 2001 *Adv. Mater.* **13** 44
[48] Colenari N F, Bradley D D C, Friend R H, Burn P L, Holmes A B and Spangler C W 1990 *Phys. Rev.* B **42** 11670
[49] Russell D M 2002 *PhD Thesis* University of Cambridge
[50] Nguyen T Q, Wu J, Doan V, Schwartz B J and Tolbert S H 2000 *Science* **288** 653
[51] Beljonne D, Poutois G, Silva C, Hennebicq E, Herz L M, Friend R H, Scholes G D, Setayesh S, Müllen K and Brédas J-L 2002 *Proc. Natl Acad. Sci. USA* **99** 10982
[52] Grell M, Bradley D D C, Ungar G, Hill J and Whitehead K S 1999 *Macromolecules* **32** 5810
[53] Frankevich E L, Lymarev A A, Sokolik I, Karasz F E, Blumstengel S, Baughman R H and Horhold H H 1992 *Phys. Rev.* B **46** 9320
[54] Cadby A J, Yang C, Holdcroft S, Bradley D D C and Lane P A 2002 *Adv. Mater.* **14** 57
[55] Wohlgenannt M, An C P and Vardeny Z V 2000 *J. Phys. Chem.* B **104** 3846